

# Ultrapure and efficient electroluminescence in alkali metal doped inorganic perovskite quantum wires arrays

Received: 5 September 2024

Accepted: 12 June 2025

Published online: 01 July 2025



Yang Bryan Cao<sup>1,2,12</sup>, Yu Fu<sup>3,12</sup>, Yu Zhou<sup>1,2,12</sup>, Xiao Qiu<sup>1,2</sup>, Daquan Zhang<sup>1,2</sup>, Yucheng Ding<sup>1,2</sup>, Ying Xie<sup>4</sup>, Beita Ren<sup>1,2</sup>, Qingsong Shan<sup>5</sup>, Pok Fung Chan<sup>6</sup>, Wenying Tang<sup>1,2</sup>, Feng Xue<sup>1,2</sup>, Xiaofei Sun<sup>1,2</sup>, Kemeng Zhou<sup>7,8</sup>, Jin-Feng Liao<sup>9</sup>, Zijin Jin<sup>10</sup>, Qianpeng Zhang<sup>1,2</sup>, Jiannong Wang<sup>10</sup>, Dai-Bin Kuang<sup>9</sup>, Xinhui Lu<sup>6</sup>, Yuanjing Lin<sup>7,8</sup>, Haibo Zeng<sup>5</sup>✉ & Zhiyong Fan<sup>1,2,11</sup>✉

Alkali metal doping has been widely utilized to regulate metal halide perovskites and improve their luminescence performance. However, due to the discordant tolerance factor caused by the smaller size of potassium and rubidium ions, it is still debatable whether they can be incorporated in the cesium perovskite crystal lattice. Here we provide unambiguous evidence for the formation of  $\text{Rb}^+$  and  $\text{K}^+$  substitutionally doped stable perovskite cubic crystal structure in the form of quantum wires embedded in nanoporous alumina template. The suppressed inner defects and enhanced exciton binding energy lead to a reduced non-radiative recombination in the co-doped perovskite quantum wires. The perovskite light-emitting diodes with a maximum external quantum efficiency of 17.5%, 21.2%, 24.9% and 30.1% and a maximum luminance of  $1638 \text{ cd m}^{-2}$ ,  $3365 \text{ cd m}^{-2}$ ,  $13,483 \text{ cd m}^{-2}$  and  $31,706 \text{ cd m}^{-2}$  for electroluminescence peak of 476 nm (primary-blue), 483 nm (sky-blue), 490 nm (sky-blue) and 512 nm (green) are fabricated respectively. Surprisingly, all devices emit high-color purity light with narrow linewidth of  $\leq 16 \text{ nm}$ .

The ease of compositional engineering for metal halide perovskite (MHPs) materials results in a wide spectrum of opto-electrical properties, facilitating their application in various research fields such as solar cells, photodetectors, light-emitting diodes and so forth<sup>1–7</sup>. Specifically, introducing alkali metal ( $\text{Li}^+$ ,  $\text{Na}^+$ ,  $\text{K}^+$ ,  $\text{Rb}^+$  and  $\text{Cs}^+$ ) into

perovskites, characterized by a typical crystal structure with the chemical formula of  $\text{ABX}_3$ , has been proven to be an effective approach to tailor their properties<sup>2,8–13</sup>. Nevertheless, only cesium cation possesses a tolerance factor value situated within the range of 0.8–1.0<sup>1</sup> among these alkali metals, ensuring the formation of a stable cubic perovskite

<sup>1</sup>Department of Electronic & Computer Engineering, The Hong Kong University of Science and Technology, Kowloon, Hong Kong SAR, China. <sup>2</sup>State Key Laboratory of Advanced Display and Optoelectronics Technologies HKUST, Kowloon, Hong Kong SAR, China. <sup>3</sup>School of Advanced Energy, Sun Yat-Sen University, Shenzhen, Guangdong, China. <sup>4</sup>School of Chemistry and Materials Science, Heilongjiang University, Harbin, Heilongjiang, China. <sup>5</sup>MIIT Key Laboratory of Advanced Display Materials and Devices, Institute of Optoelectronics & Nanomaterials, School of Materials Science and Engineering, Nanjing University of Science and Technology, Nanjing, China. <sup>6</sup>Department of Physics, The Chinese University of Hong Kong, New Territories, Hong Kong, China. <sup>7</sup>School of Microelectronics, Southern University of Science and Technology, Shenzhen, China. <sup>8</sup>State Key Laboratory of Quantum Functional Materials, Southern University of Science and Technology, Shenzhen, China. <sup>9</sup>MOE Key Laboratory of Bioinorganic and Synthetic Chemistry, Lehn Institute of Functional Materials, School of Chemistry, Sun Yat-Sen University, Guangzhou, China. <sup>10</sup>Department of Physics, The Hong Kong University of Science and Technology, Kowloon, Hong Kong SAR, China. <sup>11</sup>Department of Chemical and Biological Engineering, HKUST, Kowloon, Hong Kong SAR, China. <sup>12</sup>These authors contributed equally: Yang Bryan Cao, Yu Fu, Yu Zhou. ✉e-mail: [zeng.haibo@njust.edu.cn](mailto:zeng.haibo@njust.edu.cn); [eezf@ust.hk](mailto:eezf@ust.hk)

structure. As the neighboring alkali metal cation of  $\text{Cs}^+$ , the tolerance factors of  $\text{Rb}^+$  and  $\text{K}^+$  cations are  $-0.78$  and  $0.75^1$ , respectively, which are below the range in which the stable cubic perovskite structure can be formed. This indicates that it is difficult for them to substitute A-site cation in the perovskite crystal lattice. However, controversy remains regarding whether  $\text{Rb}^+$  and  $\text{K}^+$  cations can enter the lattice.

Indeed, noteworthy improvements on the opto-electric device performance have been made by introducing  $\text{Rb}^+$  and  $\text{K}^+$  cations into perovskites, which regulates the crystal lattice, reduces trap density, modulates the film morphology and so on<sup>2,5,11,14–17</sup>. Nonetheless, a scarcity of reports provides substantial evidence to reveal their specific position and how they affect the device performance. Currently, investigations have suggested the existence of three possible scenarios: 1.  $\text{Rb}^+$  and  $\text{K}^+$  cations are unable to enter the lattice and they instead reside at the grain boundaries in the form of  $\text{Rb}^+$ -rich or  $\text{K}^+$ -rich compounds<sup>2,11,16,18–20</sup>. 2.  $\text{Rb}^+$  and  $\text{K}^+$  cations mainly occupy the interstitial sites in the lattice<sup>15,17,21,22</sup>. 3.  $\text{Rb}^+$  and  $\text{K}^+$  cations can partially replace A-site cation in the lattice<sup>1,5,23–26</sup>. Generally, there is no definitive or universally accepted understanding regarding the specific location of  $\text{Rb}^+$  and  $\text{K}^+$  cations within the lattice and its connection to the device performance.

Here, we present substantial evidence supporting the partial substitution of A-site  $\text{Cs}^+$  cation with  $\text{Rb}^+$  and  $\text{K}^+$  cations in all-inorganic perovskite quantum wires (PeQWs) arrays. The established fact is derived from a comprehensive analysis involving multiple experimental techniques and theoretical calculations. According to the density functional theory (DFT) calculation, the co-doped PeQWs lattice structure is stabilized by the bonding between perovskite and nanoporous alumina template (NAT). Both experimental and theoretical results illustrate that doping  $\text{Rb}^+$  and  $\text{K}^+$  cations greatly suppress inner defects and enhance the exciton binding energy, which originate from an ordered perovskite lattice and a weakened Anderson localization. Consequently, perovskite light-emitting diodes (PeLEDs) based on the co-doped PeQWs arrays exhibit a peak external quantum efficiency (EQE) of 17.5%, 21.2%, 24.9% and 30.1% and a maximum luminance of  $1638 \text{ cd m}^{-2}$ ,  $3365 \text{ cd m}^{-2}$ ,  $13,483 \text{ cd m}^{-2}$  and  $31,706 \text{ cd m}^{-2}$  for blue or green emission at the electroluminescence (EL) peak of 476 nm (primary-blue), 483 nm (sky-blue), 490 nm (sky-blue) and 512 nm (green). Intriguingly, the EL full width at half maximum (FWHM) values are 14.3 nm (primary-blue), 14.8 nm (sky-blue), 15.0 nm (sky-blue) and 16.0 nm (green) which are narrow among high-efficiency PeLEDs reported in literature, to our best knowledge. These results substantiate that incorporating  $\text{Rb}^+$  and  $\text{K}^+$  cations in PeQWs arrays ensures excellent efficiency, luminance and color purity simultaneously.

## Results

### Substituting Cs with alkali metals at A-site in perovskite

Initially, we fabricate all-inorganic PeQWs arrays through a template-assisted solution method<sup>27</sup>. The perovskite precursor solutions are prepared by mixing  $\text{ABr}$  and  $\text{PbX}_2$  ( $\text{A} = \text{Rb}$ ,  $\text{K}$  or  $\text{Cs}$ ;  $\text{X} = \text{Br}$  or  $\text{Cl}$ ) in dimethyl sulfoxide (DMSO). The fabrication process is a high throughput single-step spin-coating process (Fig. 1a). As expected, the cross-sectional scanning electron microscopy (SEM) image in Fig. 1a reveals the presence of vertically aligned PeQWs arrays with a thickness of  $\sim 100 \text{ nm}$ . Additionally, transmission electron microscopy (TEM) is also employed to examine the crystal orientation of single PeQW (Supplementary Fig. 1a–d). Observation reveals a high-crystallinity PeQW with a consistent orientation spanning a length of 40–50 nm, strongly suggesting the likelihood of single PeQW being single crystal.

Several techniques are then utilized to determine the precise occupying locations of  $\text{Rb}^+$  and  $\text{K}^+$  cations in the PeQW, including low-dose high-resolution transmission electron microscopy (HRTEM), grazing-incidence wide-angle X-ray scattering (GIWAXS), X-ray

diffraction (XRD) and X-ray photoelectron spectroscopy (XPS). Firstly, the pristine  $\text{CsPbBr}_3$  QWs are set as control samples. Figure 1b displays the HRTEM image of pristine  $\text{CsPbBr}_3$  QWs, demonstrating their typical cubic perovskite structure projected along  $\langle 100 \rangle$  direction, along with the corresponding atomic structure. The fast Fourier transform (FFT) diffractogram in the inset of Fig. 1b confirms the presence of the plane in pristine  $\text{CsPbBr}_3$  QWs while the average interplane spacing between two neighboring (100) planes is measured to be  $6.06 \text{ \AA}$ . The crystal lattice in the edge and middle of a single pristine  $\text{CsPbBr}_3$  QW are depicted in the selected zoom-in HRTEM images presented in Fig. 1c, d. In addition to three-dimensional cubic  $\text{CsPbBr}_3$  phase, the existence of zero-dimensional  $\text{Cs}_4\text{PbBr}_6$  phase is also observed in pristine PeQWs, as shown in Supplementary Fig. 2a–d.

For target PeQWs,  $\text{Rb}^+$  and  $\text{K}^+$  cations are doped into the pristine  $\text{CsPbBr}_3$  QWs. To verify the success of  $\text{Rb}^+$  and  $\text{K}^+$  cations doping, XPS analysis and energy-dispersive X-ray spectroscopy (EDS) mapping of  $\text{Rb}^+$ ,  $\text{K}^+$ : $\text{CsPbBr}_3$  QWs arrays were collected (Fig. 1e and Supplementary Fig. 3a–l). The Rb 3d spectrum for  $\text{Rb}^+$ ,  $\text{K}^+$ : $\text{CsPbBr}_3$  PeQWs exhibits two dominant peaks located at 110.20 eV and 111.51 eV, corresponding to  $3d_{5/2}$  and  $3d_{3/2}$  orbitals, respectively. In the K 2p spectrum, two K binding energy peaks are observed, which are associated with the  $2p_{3/2}$  (293.29 eV) and  $2p_{1/2}$  (296.10 eV) levels. In stark contrast, the elemental profiles of the Rb (Supplementary Fig. 3i) and K (Supplementary Fig. 3j) elements are evident in the profiles of the  $\text{Rb}^+$ ,  $\text{K}^+$ : $\text{CsPbBr}_3$  PeQWs arrays, whereas these profiles were not detected in the pristine  $\text{CsPbBr}_3$  arrays (Supplementary Fig. 3c, d). Some studies point out that  $\text{Rb}^+$  and  $\text{K}^+$  cations tend to accumulate at the grain boundaries in the form of  $\text{Rb}^+$ -rich or  $\text{K}^+$ -rich compounds, such as  $\text{RbPbX}_3$ ,  $\text{K}_2\text{PbX}_4$ , and  $\text{KX}^{2,16,18–20,28}$ . However, in our case, the XRD peak corresponding to these compounds is not identifiable in the XRD patterns depicted in Fig. 1f, which means these compounds don't exist in the  $\text{Rb}^+$ ,  $\text{K}^+$ : $\text{CsPbBr}_3$  PeQWs arrays. Meanwhile, the distinctive peaks, which are classified to (100), (110) and (200) planes, undergo a noticeable shift towards a larger angle as the  $\text{Rb}^+$  and  $\text{K}^+$  cations are sequentially doped in PeQWs. This proves that the  $\text{Rb}^+$  and  $\text{K}^+$  cations doping leads to a lattice contraction which is consistent with previous studies that support  $\text{Rb}^+$  and  $\text{K}^+$  cations substituting A-site cation<sup>1,5,23,25</sup>. Moreover, the GIWAXS patterns and radial integration of 2D GIWAXS exhibit the same trend as that observed in the XRD patterns (Fig. 1g). From the HRTEM image of  $\text{Rb}^+$ ,  $\text{K}^+$ : $\text{CsPbBr}_3$  PeQWs (Fig. 1h), a perfect cubic structure projected along  $\langle 110 \rangle$  direction is pictured. The average interplane distance of two neighboring (100) planes decreases to  $5.97 \text{ \AA}$  which coincides with the XRD and GIWAXS results. Although some researchers also claim that interstitial occupancy of  $\text{Rb}^+$  and  $\text{K}^+$  cations is dominant<sup>15,17,21,22,26</sup>, there is no sign of  $\text{Rb}^+$  or  $\text{K}^+$  cations positioning at the interstitial site in the crystal lattice (Fig. 1i, j). In addition, the intensity profiles of various atoms at different positions are provided, as illustrated in Supplementary Fig. 4a–d. And yet, these atoms are precisely in their designated positions, devoid of occupying the interstitial site. Generally, the available evidence strongly indicates that  $\text{Rb}^+$  and  $\text{K}^+$  cations can replace  $\text{Cs}^+$  cation at A-site in the PeQWs.

### The formation energy of alkali metals substituting Cs

We then perform DFT calculations to bolster our rationale and elucidate the impact it has on material properties. Firstly, a computational model of  $\text{CsPbBr}_3$  without  $\text{Al}_2\text{O}_3$  (Fig. 2a) is constructed to calculate the formation energy of Rb and K atoms replacing Cs atom at A-site. The detailed simulation processes are shown in Supplementary Fig. 5. Since Rb and K atoms are smaller than Cs atom and beyond the tolerance of the perovskite structure, the formation energy of Rb and K atoms displacing Cs atom at A-site is 0.303 eV and 0.537 eV (Fig. 2b), respectively. Such a high formation energy implies that Rb and K cannot be easily dissolved in the perovskite structure. Then  $\text{Al}_2\text{O}_3$  is introduced to the computational model of  $\text{CsPbBr}_3$  (Fig. 2c)<sup>29</sup>. In the simulation processes (Supplementary Figs. 6, 7), Cs atom in the bulk

and at the interface between  $\text{CsPbBr}_3$  and  $\text{Al}_2\text{O}_3$  was substituted by Rb and K atoms. Surprisingly, as shown in Fig. 2d, e and Supplementary Fig. 7b, the formation energy of Rb and K atoms replacing Cs atom at

A-site has been reduced significantly compared with the model without  $\text{Al}_2\text{O}_3$ , making it possible for Rb and K atoms to be incorporated in the perovskite structure. This result is consistent with our

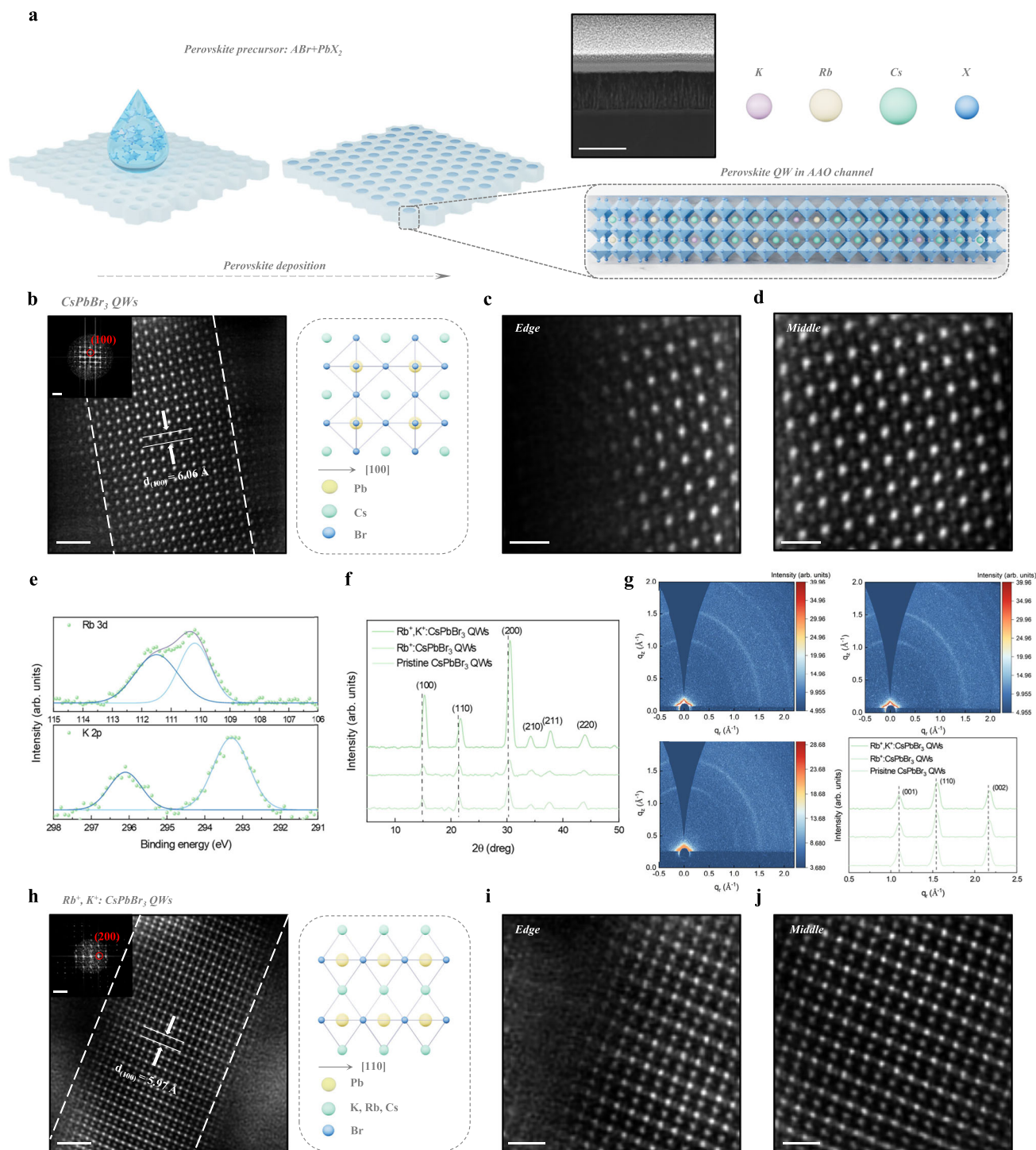


**Fig. 1 | Substitution of Cs with Rb and K at A-site in alkali metals doped PeQW arrays.** **a** Schematic illustration of the fabrication of alkali metals doped PeQW arrays and substitution of Cs with Rb and K at A-site in PeQW. Inset, cross-sectional TEM image of PeQW arrays. Scale bar, 200 nm. **b** Atomically resolved low-dose HRTEM image of single pristine  $\text{CsPbBr}_3$  QW with atomic structure model projected along  $\langle 100 \rangle$  direction. Scale bar, 2 nm. Inset, fast Fourier transform diffractograms showing the cubic lattice structure. Scale bar,  $2 \text{ nm}^{-1}$ . **c, d** Zoom-in low-dose HRTEM image of perovskite lattice in the edge and middle of pristine  $\text{CsPbBr}_3$  QW. Scale bar, 1 nm. **e** Rb 3d and K 2p XPS core-level

spectra of  $\text{Rb}^+$ ,  $\text{K}^+$ :  $\text{CsPbBr}_3$  QWs. **f** XRD pattern of pristine  $\text{CsPbBr}_3$  QW,  $\text{Rb}^+$ :  $\text{CsPbBr}_3$  QWs and  $\text{Rb}^+$ ,  $\text{K}^+$ :  $\text{CsPbBr}_3$  QWs. **g** GIWAXS pattern and in-plane intensity profiles extracted from the GIWAXS of pristine  $\text{CsPbBr}_3$  QW,  $\text{Rb}^+$ :  $\text{CsPbBr}_3$  QWs and  $\text{Rb}^+$ ,  $\text{K}^+$ :  $\text{CsPbBr}_3$  QWs. **h** Atomically resolved low-dose HRTEM image of single pristine  $\text{CsPbBr}_3$  QW with atomic structure model projected along  $\langle 110 \rangle$  direction. Scale bar, 2 nm. Inset, fast Fourier transform diffractograms showing the cubic lattice structure. Scale bar,  $5 \text{ nm}^{-1}$ . **i, j** Zoom-in low-dose HRTEM image of perovskite lattice in the edge and middle of  $\text{Rb}^+$ ,  $\text{K}^+$ :  $\text{CsPbBr}_3$  QWs. Scale bar, 1 nm.



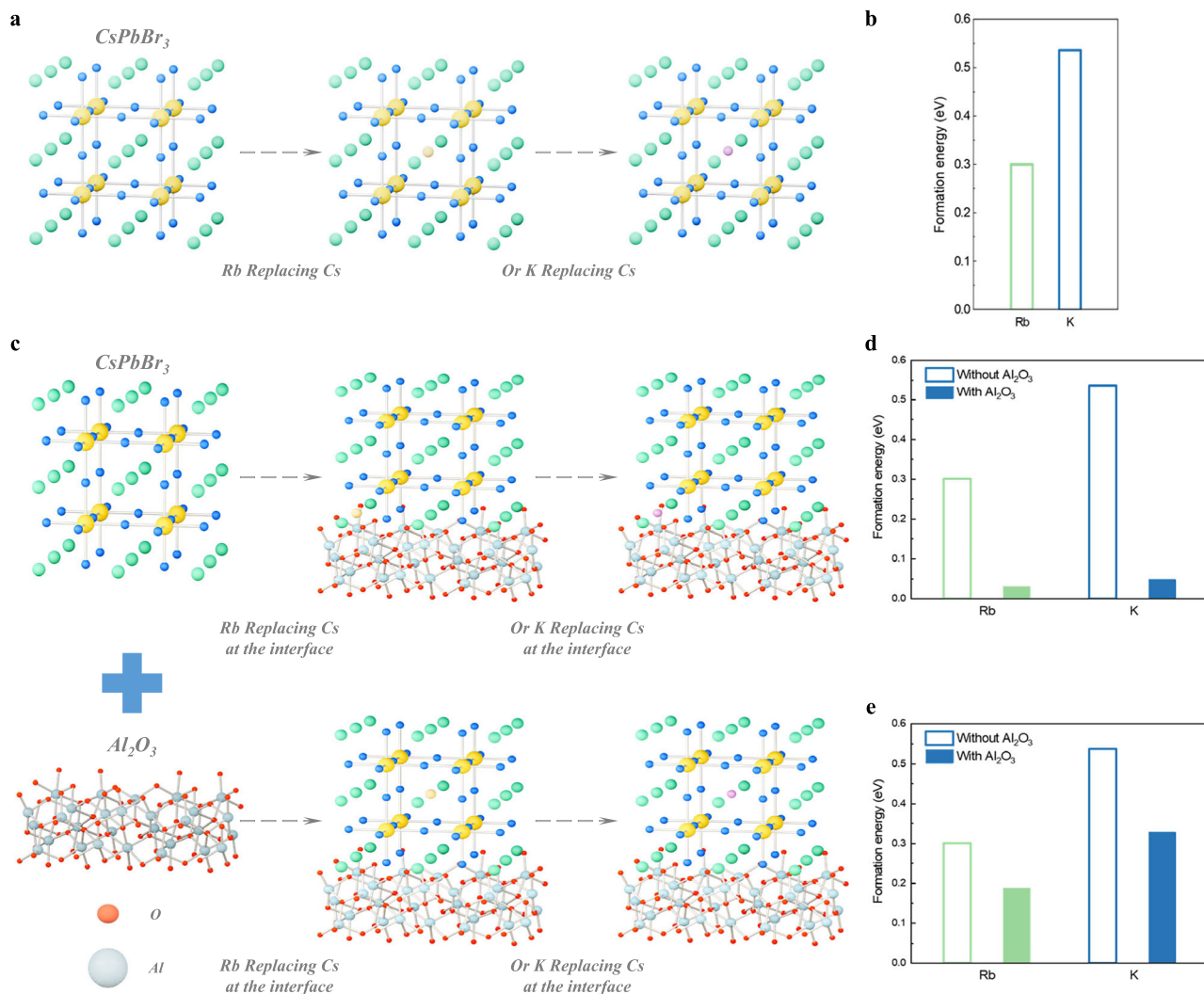


**Fig. 2 | DFT calculation of formation energy for the substitution of Cs with Rb and K at A-site. a** Schematic drawing of Rb or K replacing Cs at A-site in the model without  $\text{Al}_2\text{O}_3$ . **b** Formation energy of Rb or K replacing Cs at A-site. **c** Schematic

drawing of Rb or K replacing Cs at A-site in the model with  $\text{Al}_2\text{O}_3$ . **d** Formation energy of Rb or K replacing Cs at A-site in the bulk of  $\text{CsPbBr}_3$ . **e** Formation energy of Rb or K replacing Cs at A-site at the interface of  $\text{CsPbBr}_3$  and  $\text{Al}_2\text{O}_3$ .

experimental observation that Rb and K cations can reside at A-site in the perovskite lattice of all-inorganic PeQWs arrays. It is known that replacing Cs atom in  $\text{CsPbBr}_3$  at A-site by using Rb or K atom introduces large distortion of the cubic lattice, causing lattice instability and phase transformation<sup>19,20</sup>. However, in our scenario, when  $\text{CsPbBr}_3$  is embedded in the NAT, Br-Al and Pb-O bonds are formed (Supplementary Figs. 6, 7) at the  $\text{Al}_2\text{O}_3/\text{CsPbBr}_3$  interface<sup>27,29</sup>. These bonds help to stabilize the perovskite lattice upon doping of Rb or K, even though there is a lattice mismatch. As the PeQW has a very small diameter (~6.4 nm), this interface effect can dominate the entire PeQW, making Rb and K doping more stable inside PeQW as compared to that inside a bulk/film of perovskite<sup>30,31</sup>. Based on the prior report<sup>32</sup>, the interference between electron's multiple scatterings by random defects in the potential will induce Anderson localization. Rb and K atoms staying at the interstitial site will definitely destroy the ordering of perovskite lattice, resulting in Anderson localization. On the contrary, Rb and K atoms replacing Cs atom at A-site will not damage the orderliness of perovskite lattice and contribute to positive impact on the material properties which will be demonstrated subsequently.

### Properties of alkali metals doped perovskite quantum wires

Intriguingly, we have not only achieved green emission but also extended our approach to include blue emission simply through the process

of chloride doping. XRD and GIWAXS measurements (Fig. 3a and Supplementary Fig. 8) show diffraction peaks indexed to the cubic perovskite structure. The XPS analysis is studied to confirm the existence of each chemical element (Supplementary Fig. 9). The corresponding steady state PL spectra of  $\text{Rb}^+$ ,  $\text{K}^+$ : $\text{CsPbBr}_3$  and  $\text{Rb}^+$ ,  $\text{K}^+$ : $\text{CsPb}(\text{Br}_{1-x}\text{Cl}_x)_3$  QWs are shown in Fig. 3b, exhibiting peaks at 476 nm (primary-blue), 483 nm (sky-blue), 490 nm (sky-blue) and 512 nm (green), respectively. Surprisingly, the photoluminescence (PL) FWHMs of corresponding PeQWs are measured to be 15.1 nm, 15.4 nm, 15.7 nm, 17.1 nm, showcasing an exceptional level of color purity. In comparison, the FWHM is ~17.6 nm and 18.0 nm for pristine PeQWs (Supplementary Fig. 10a, b). The Ultraviolet-visible (UV-Vis) absorbance spectra are also summarized in Supplementary Fig. 10. The transient absorption (TA) spectra exhibit a pronounced single bleaching peak and the peak position remains nearly constant over time (Supplementary Figs. 11–13 and Supplementary Table 1). The Urbach energy ( $E_u$ ) is calculated from the absorption coefficient spectra (Supplementary Fig. 14) extracted from the absorbance spectra as follows:

$$\alpha = \alpha_0 e^{\frac{h\nu}{E_u}} \quad (1)$$

where  $\alpha$  is the absorption coefficient and  $h\nu$  is the photon energy<sup>33</sup>. The reduction in the  $E_u$  value from >30 meV to ~20 meV indicates a low

electronic disorder in the band edges<sup>34</sup> for Rb<sup>+</sup> and K<sup>+</sup> doped PeQWs which can be partially attributed to the elimination of zero-dimensional Cs<sub>4</sub>PbBr<sub>6</sub> phase whose presence cannot be found in the HRTEM images.

A time-resolved photoluminescence (TRPL) measurement is performed to examine the lifetime of excited charge carriers (Fig. 3c). The PL decay curves are fitted into two regions, with a short lifetime ( $\tau_1$ ) associated with trap-mediated nonradiative recombination, and a longer lifetime ( $\tau_2$ ) ascribed to radiative recombination (Supplementary Fig. 15 and Supplementary Table 2)<sup>35</sup>. The incorporation of Rb<sup>+</sup> and K<sup>+</sup> leads to an extension of both  $\tau_1$  and  $\tau_2$  in compared with the pristine PeQWs, implying Rb<sup>+</sup> and K<sup>+</sup> doped PeQWs possess a lower defect density and an enhanced radiative recombination. To investigate the defect density and the radiative recombination in Rb<sup>+</sup> and K<sup>+</sup> doped PeQWs, space charge-limited current (SCLC) measurements (Supplementary Figs. 16–18) are conducted based on hole-only and electron-only devices. Additionally, temperature-dependent steady-state PL spectra measurements (Supplementary Fig. 19) are also carried out. The equation as below is used to calculate the total trap-state density inside the PeQWs:

$$n_t = \frac{2\epsilon\epsilon_0 V_{\text{TFL}}}{eL^2} \quad (2)$$

where  $n_t$  is the trap state density,  $V_{\text{TFL}}$  is the trap-filled limit voltage,  $L$  is the thickness of the perovskites,  $e$  is the elementary charge,  $\epsilon_0$  and  $\epsilon$  are the vacuum permittivity and relative permittivity, respectively<sup>36</sup>. The significant reduction in the trap-state density provides evidence that the inclusion of RbBr and KBr in PeQWs effectively heal the Cs and halide vacancies, thereby contributing to an increased luminescence efficiency. The confirmation of improved radiative recombination is achieved through temperature-dependent steady-state PL analysis. The exciton binding energy ( $E_b$ ) is estimated to be 352 meV, 343 meV, 332 meV and 236 meV for Rb<sup>+</sup>, K<sup>+</sup>: CsPb(Br<sub>1-x</sub>Cl<sub>x</sub>)<sub>3</sub> and Rb<sup>+</sup>, K<sup>+</sup>: CsPbBr<sub>3</sub> QWs, significantly surpassing those reported in our previous study<sup>27</sup> and in other literatures employing perovskite as emissive layer. Such a high  $E_b$  value indicates Rb<sup>+</sup> and K<sup>+</sup> doped PeQWs experience a strong quantum confinement effect due to the ultra-small size. The reduction in defect density and the contraction of perovskite lattice after doping also contribute to the enhanced exciton binding energy. The fluence-dependent TA measurements are performed to study the charge-carriers dynamics for cross-check (Supplementary Fig. 20 and Supplementary Table 3). Consistent with the results in another paper<sup>37</sup>, the  $k_1$  of PeQWs is two orders of magnitude higher than that of bulk perovskite. The  $k_1$  of PeQWs is dominated by geminate exciton recombination while the  $k_1$  of bulk perovskite is dominated by trap-assisted Shockley–Read–Hall (SRH) nonradiative recombination. Moreover, the PeQWs exhibit higher radiative recombination rate compared with bulk perovskite. Because of enhanced exciton-exciton interactions, the obtained Auger recombination rate of PeQWs is one order of magnitude higher. Consequently, Rb<sup>+</sup> and K<sup>+</sup> doped PeQWs show an increased photoluminescence quantum yield (PLQY) of 66.2%, 71.5%, 81.6% and 96.0% for different emission wavelengths (Fig. 3d).

In strongly coupled material systems such as quantum dots or nanoplates<sup>38,39</sup>, the variation in size and interdot/interplate distance, quantum dots/nanoplates organization and defects on interface will generate bandtail states and mid-gap trap states, leading to a strong Anderson localization. However, even though the PeQWs diameter has a large variation, and they are not perfectly vertical aligned on the substrate, the coupling between PeQWs is weak since they are embedded in NAT and the pitch of NAT pores is more than 10 nm<sup>40</sup>. Hence, the adverse effect of Anderson localization in strongly coupled material system can be avoided. Moreover, with Rb and K atoms replacing Cs atom at A-site instead of situating at the interstitial site as well as healing Cs and halide defects at the interface, the lattice order is

restored, resulting in a weak Anderson localization. Furthermore, previous study also shows that the formation of Cs and alkali metal cation alloy alters the supersaturation of Cl-rich domains and/or increases the formation energy of perovskites, leading to an excellent compositional homogeneity<sup>41</sup>. Consequently, the excellent compositional homogeneity results in a narrower emission linewidth. In general, we conclude that the narrow emission linewidth and high exciton binding energy can be attributed to the weakened Anderson localization and the improved compositional homogeneity based on the above discussion.

To evaluate the environmental PL stability under ambient condition (24 °C and 10–20% relative humidity) of the Rb<sup>+</sup> and K<sup>+</sup> doped PeQWs arrays, time-dependent normalized PL tests are performed (Fig. 3e). Remarkably, Rb<sup>+</sup> and K<sup>+</sup> doped PeQWs arrays have an extraordinary  $T_{95}$  PL lifetime of over 1000 h.

### High-performance perovskite light-emitting diodes

Encouraged by the benefits from Rb<sup>+</sup> and K<sup>+</sup> cations doping, we successfully manufacture PeLEDs based on the Rb<sup>+</sup> and K<sup>+</sup> doped PeQWs arrays (Supplementary Fig. 21). The device comprises a layered structure of conducting indium tin oxide (ITO)/1,4,5,8,9,11-Hexaazatriphenylenehexacarbonitrile (HAT-CN)/1,3,5-tris (bromomethyl) benzene (TBB) doped 1,1-Bis[(di-4-tolylamino)phenyl]cyclohexane (TAPC)/PeQWs arrays/aluminum oxide (Al<sub>2</sub>O<sub>3</sub>)/aluminum (Al) as schematically shown in Fig. 4a, b. The flat-band energy band diagram, derived from the ultraviolet photoelectron spectroscopy (UPS) measurements (Supplementary Fig. 22 and Supplementary Table 4), is illustrated in Fig. 4c. In contrast to the pristine PeQWs, the Rb<sup>+</sup> and K<sup>+</sup> doped PeQWs demonstrate a shallower valence band level, favoring the hole injection from TAPC to PeQWs. The EL spectra, corresponding Commission Internationale de l'éclairage (CIE) chromaticity coordinate diagram and angular electroluminescence distribution are depicted in Fig. 4d, e and Supplementary Fig. 23. Remarkably, the PeLEDs based on the Rb<sup>+</sup> and K<sup>+</sup> doped PeQWs arrays show an EL peak centered at 476 nm (primary-blue), 483 nm (sky-blue), 490 nm (sky-blue) and 512 nm (green), with a narrow FWHM of 14.3 nm, 14.8 nm, 15.0 nm and 16.0 nm, respectively. These FWHM values are quite narrow among high-efficiency PeLEDs (Supplementary Fig. 24), to our best knowledge. The corresponding CIE chromaticity coordinates are (0.101, 0.122), (0.077, 0.183), (0.047, 0.323) and (0.040, 0.780), exhibiting high color-purity with a calculated value of as high as 99.1% (Supplementary Fig. 25 and Supplementary Table 5).

Furthermore, the finite-difference-time-domain (FDTD) simulations (Supplementary Figs. 26–28 and Supplementary Table 6) verify that our PeLEDs can reach a light out-coupling efficiency (OCE) of 85% which is 4 times higher than planar structure PeQWs with only ~20% OCE<sup>27,42</sup>. The detailed current density ( $J$ )-voltage ( $V$ )-luminance ( $L$ ) characteristics are summarized in Fig. 4f, Supplementary Fig. 29 and Supplementary Tables 7, 8. The PeLEDs show a maximum luminance of 1638 cd m<sup>-2</sup> (primary-blue), 3365 cd m<sup>-2</sup> (sky-blue), 13,483 cd m<sup>-2</sup> (sky-blue) and 31,706 cd m<sup>-2</sup> (green). From the external quantum efficiency (EQE)-luminance ( $L$ ) curves (Fig. 4g, h), the PeLEDs attain a peak EQE value of 17.5% (primary-blue), 21.2% (sky-blue), 24.9% (sky-blue) and 30.1% (green). Besides, the EQEs distribution is reported in Fig. 4i and Supplementary Fig. 30, showing great reproducibility.

Finally, the devices stability is analyzed by separately subjecting them to different electric bias and a constant driving current. The EL spectra remain unchanged under varying applied voltages up to 12 V (Supplementary Fig. 31), suggesting that the devices have extraordinary spectral stability against high working voltage. To expedite the aging process, the initial luminance is deliberately set to 1000 cd m<sup>-2</sup>. The operating half lifetimes ( $T_{50}$ ) are 38 s (primary-blue), 58 s (sky-blue), 370 s (sky-blue) and 1325 s (green), respectively. Impressively, the EL wavelength and FWHM keep consistent throughout the operation.

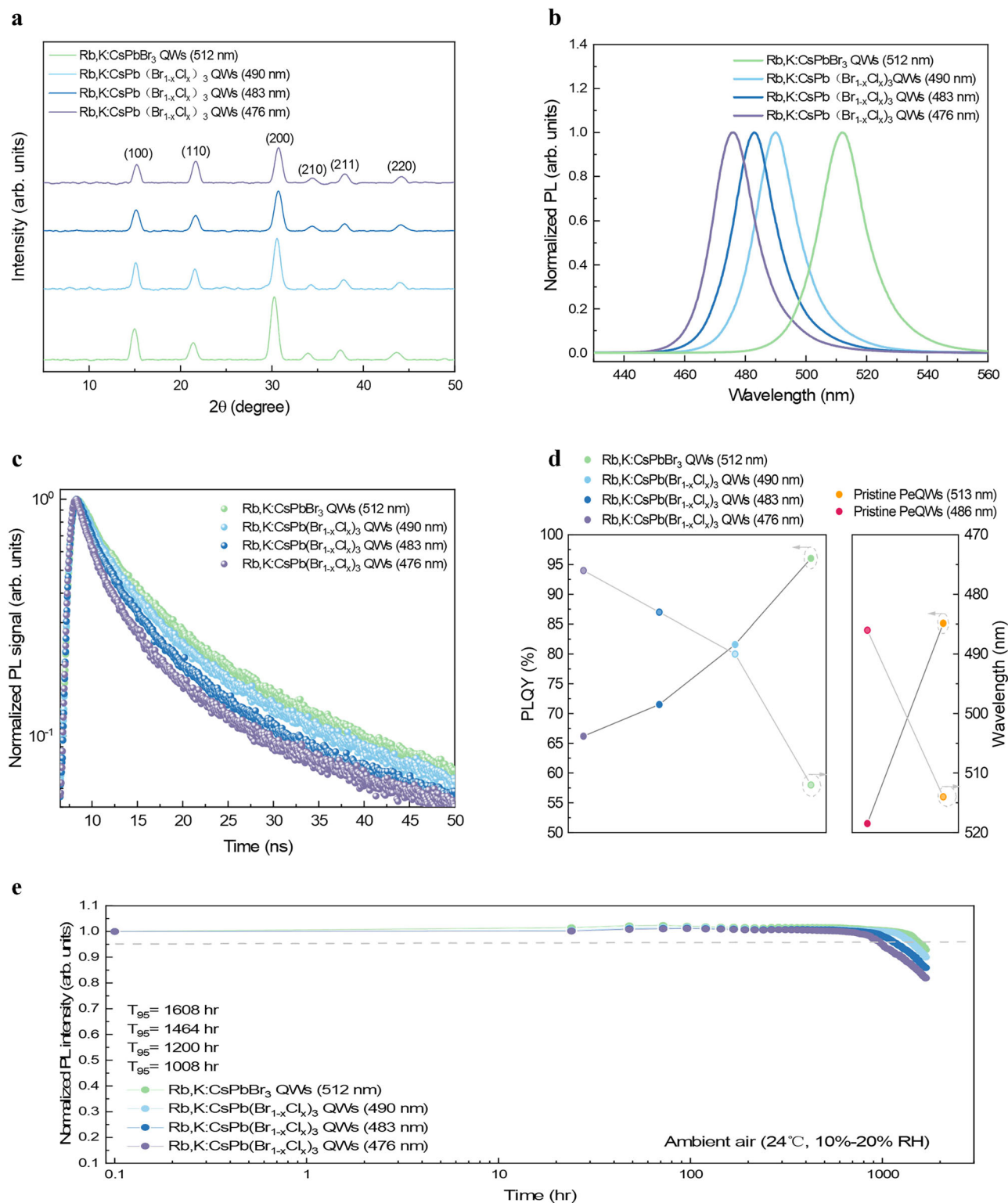


**Fig. 3 | Properties of alkali metals doped PeQW arrays. a** XRD patterns, **b** Normalized photoluminescence spectra ( $\lambda_{\text{ex}} = 350\text{ nm}$ ), **c** TRPL decay curves and **d** PLQYs ( $\lambda_{\text{ex}} = 365\text{ nm}$ ) measured at corresponding photoluminescence peak of as-

synthesized alkali metals doped PeQWs. **e** Environmental photoluminescence stability under ambient condition for alkali metal doped PeQWs.

## Discussion

In conclusion, we reveal concrete evidence, including multiple experimental techniques and theoretical calculations, on that Rb and K cations can reside at A-site in the perovskite lattice of all-inorganic PeQWs arrays, preserving the order of perovskite lattice and avoiding

detrimental effects caused by Anderson localization. In virtue of DFT calculation results, we attribute the stabilized lattice structure of co-doped PeQWs to the bonding between perovskite and NAT. The improved perovskite quality enables reduced trap density, narrowed emission linewidth, enhanced exciton binding energy and increased



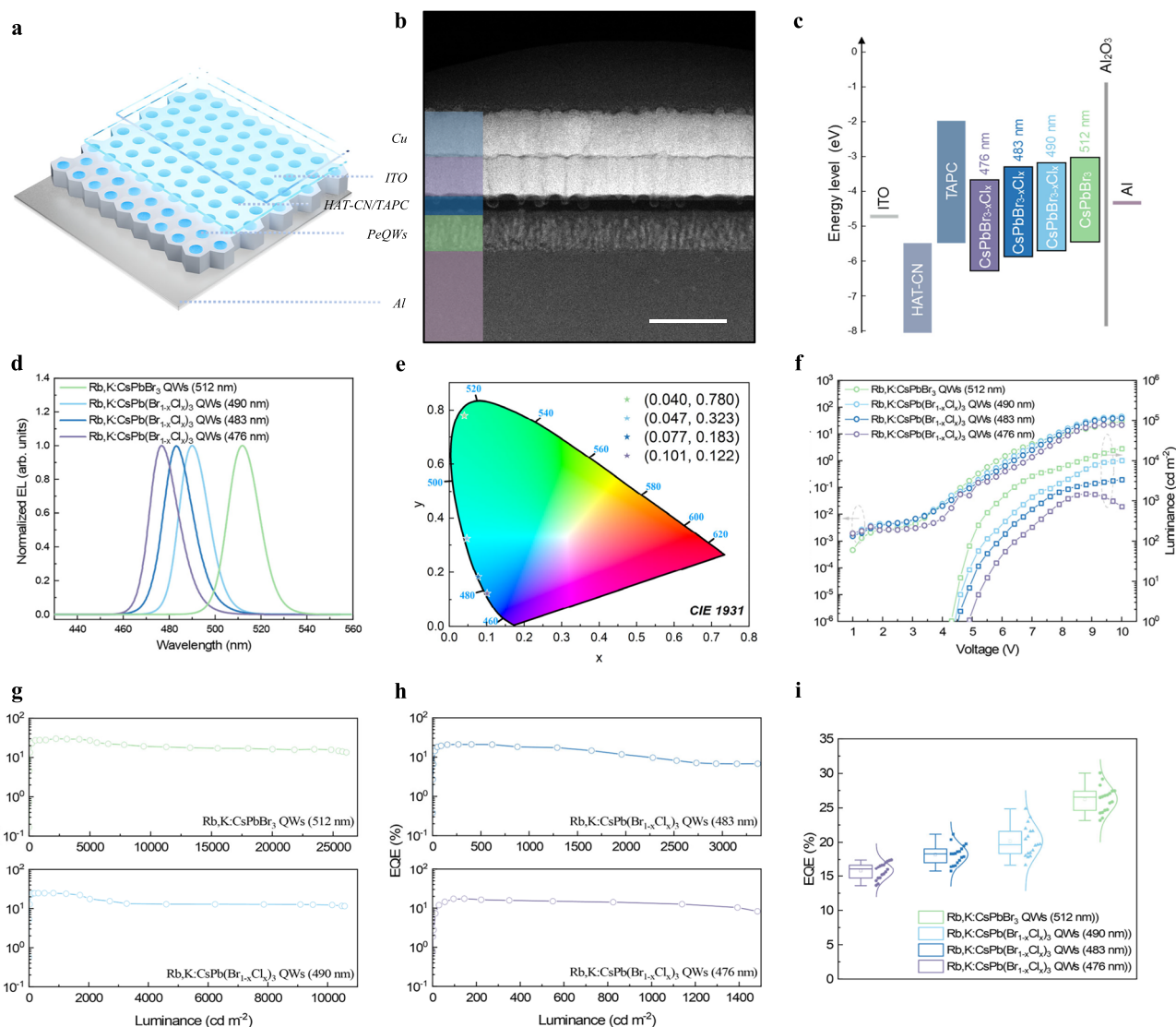


**Fig. 4 | Characteristics of PeLEDs based on alkali metals doped PeQW arrays.**

**a** Schematic of alkali metals doped PeQWs-based LED architecture. **b** Cross-sectional SEM image of a device. The thickness of each layer, which can be confirmed by SEM, are shown below: Al electrode/Al<sub>2</sub>O<sub>3</sub> hole blocking layer (~5 nm)/PeQWs emission layer (90 nm)/TAPC hole transporting layer (20 nm)/HAT-CN hole injecting layer (20 nm)/ITO transparent electrode (90 nm). Scale bar, 200 nm.

**c** Energy band diagram of each layer in PeLEDs. **d** Normalized electroluminescence spectra of blue and green PeLEDs. **e** The corresponding CIE coordinates of blue and green PeLEDs. **f** Current density (*J*)-voltage (*V*)-luminance (*L*) curves. **g, h** External quantum efficiency (EQE)-luminance (*L*) curves. **i** The EQEs distribution collected from 72 devices. The average peak EQEs are 15.8%, 18.2%, 20.2% and 26.2% with relative standard deviations of 7.7%, 7.3%, 11.1% and 7.3%, respectively.

luminous efficiency. As a result, simultaneously ultrapure and efficient PeLEDs with narrow linewidth of  $\leq 16$  nm and maximum external quantum efficiency exceeding 20% (blue) and 30% (green) are demonstrated. This fundamental progress represents a significant advancement toward achieving both high color purity and high efficiency in PeLEDs, providing a clear pathway for PeLEDs suitable for wide-color-gamut display applications.

## Methods

### Materials

Cesium bromide (CsBr, 99.999%), rubidium bromide (RbBr, 99.6%), potassium bromide (KBr,  $\geq 99\%$ ), lead bromide (PbBr<sub>2</sub>, 99.999%), lead chloride (PbCl<sub>2</sub>, 99.999%), 1,3,5-tris (bromomethyl) benzene (TBB, 97%), chlorobenzene (C<sub>6</sub>H<sub>5</sub>Cl, 99.8%) and dimethyl sulfoxide (DMSO,  $\geq 99.9\%$ ) were purchased from Sigma Aldrich. 1,1-Bis[(di-4-tolylamino)phenyl]cyclohexane (TAPC,  $>99.5\%$ ) and 1,4,5,8,9,11-Hexaazatriphenylenehexacarbonitrile (HAT-CN,  $>99\%$ ) were purchased from Ossila. Note that all materials were used without further processing.

### Preparation of the perovskite solution

The alkali metal doped perovskite precursors (K<sup>+</sup>, Rb<sup>+</sup>: CsPb(Br<sub>1-x</sub>Cl<sub>x</sub>)<sub>3</sub>) were prepared by dissolving stoichiometric ratios of each of KBr, RbBr, CsBr, PbBr<sub>2</sub> and PbCl<sub>2</sub> into DMSO at a concentration of 0.1 M. The molar ratio is KBr:RbBr:CsBr:PbBr<sub>2</sub>:PbCl<sub>2</sub> = 0.2:0.3:1:1-*x*:*x*, where *x* is 0, 0.5, 0.6 and 0.7 for different emission wavelength. In the case of precursor solutions for control samples, the molar ratio is CsBr:PbBr<sub>2</sub>:PbCl<sub>2</sub> = 1:1-*x*:*x*. The precursor solutions were stirred at 60 °C for 12 h in an N<sub>2</sub>-filled glovebox and filtered by 0.45-μm poly(tetrafluoroethylene) filters before use.

### Nanoporous alumina templates fabrication

The NAT were fabricated through a low-voltage anodic anodization process which can be found in our earlier work<sup>27,29,40</sup>. Briefly, aluminum chips of high purity with an area of  $2 \times 2.5$  cm<sup>2</sup> were sonicated in acetone and 2-propanol for 10 min each sequentially. Afterward, the aluminum chips were electro-polished at room temperature in a blended solution comprising 25 vol% perchloric acid and 75 vol%

absolute ethanol at 18 V for 3 min to achieve a smooth surface. Subsequently, anodization at 5 V took place in a 5 vol% H<sub>2</sub>SO<sub>4</sub> solution for 8 min to form 90 nm-thick porous aluminum oxide with ~6.4 nm pore diameter. Finally, the NAT were washed with deionized water and dried using compressed air.

### Perovskite light-emitting diodes fabrication

Following the fabrication of NAT, the pristine 2 × 2.5 cm<sup>2</sup> NAT were transferred into a N<sub>2</sub>-filled for PeLEDs fabrication. The filtered perovskite precursor solutions were dropped on NAT and then spin-coated at 5000 rpm for 50 s, followed by baking at 80 °C for 10 min. After annealing, the TBB doped TAPC solution (in chlorobenzene) was spin-coated on NAT filled with perovskite at 3000 rpm for 30 s. Samples were then transferred to the vacuum chamber for 20 nm HAT-CN evaporation (1 Å s<sup>-1</sup>). Finally, a 90 nm layer of ITO was magnetically sputtered at a rate of 1 Å s<sup>-1</sup> using 70 W of RF sputtering. The active device area of 0.04 cm<sup>2</sup> was defined by a shadow mask employed throughout the ITO sputtering process.

### Characterization

A Dual Beam FIB/SEM system (FEI Helios G4 UX) was used to obtain Top-view SEM images. TEM images were taken from a transmission electron microscope (TEM) JEOL (2010F). XRD patterns were collected from a Bruker D8 X-ray diffractometer. The PL spectrum, PLQY and TRPL were measured on an Edinburgh Instruments FLS920P. J.A. Woollam M-2000VI Spectroscopic Ellipsometer and Lambda 1050+ (PerkinElmer) was used to obtain Complex refractive indices (*n*, *k*) and UV-vis absorption of sample. The TA absorption spectrum was recorded on a Helios (Ultrafast Systems LLC) spectrometer equipping a sapphire laser source (Coherent Legend, 800 nm, 150 fs, 5 mJ per pulse, and 1 kHz repetition rate). A BaB<sub>2</sub>O<sub>4</sub> (BBO) crystal was used to double the frequency of 75% of the 800 nm output pulse, generating 400 nm pump light. At the same time, to produce white light continuum (420–780 nm) probe light, 25% of the output pulse was concentrated into a sapphire window. The 400 nm pump beam with a beam waist of about ~360 μm was focused on the sample and the power intensity was fixed at 40 μJ cm<sup>-2</sup>. XPS and UPS spectrum were characterized from a Kratos Axis Ultra DLD multi-technique surface analysis system. Temperature-dependent PL measurements were performed on the QE-Pro spectrometer (Ocean Insight) and Newton 920 CCD (Oxford Instruments). Atomic-scale structure imaging and chemical analysis of the samples were taken from a double Cs-corrected (S) TEM systems (FEI Themis Z, ThermoFisher Scientific) equipped with EDS (Super-X EDS system). GIWAXS measurements were accomplished with a Xeuss 2.0 WAXS/SAXS laboratory beamline using a Cu X-ray source (8.05 keV, 1.54 Å) and a Pilatus3R 300 K detector. The surface roughness of samples was measured in ambient condition via an atomic force microscope (AFM) (Bruker Dimension XR, United States) using a back side Al 100 nm coating tip (Bruker: OTESPA-R3; k: 26 N/m; f<sub>0</sub>: 300 kHz).

### Perovskite light-emitting diodes measurement

The performance of the fabricated PeLEDs was measured in ambient air without encapsulation using a Keithley 2450 source-meter unit and a calibrated Ocean Optics Flame spectrometer with an integrating sphere. The operational lifetime was monitored under constant-current conditions by the same set-up mentioned above. Cross-checking of device's EL characteristics was also conducted with a luminance meter (Konica Minolta, CS-200) and an integrated system with sphere and photomultiplier tubes (Enlitech, LQ-50X-EL).

### Data availability

The data that support the findings of this study are provided in the main text and the Supplementary Information. More data are available from the corresponding author upon request.

## References

- Saliba, M. et al. Incorporation of rubidium cations into perovskite solar cells improves photovoltaic performance. *Science* **354**, 206–209 (2016).
- Abdi-Jalebi, M. et al. Maximizing and stabilizing luminescence from halide perovskites with potassium passivation. *Nature* **555**, 497–501 (2018).
- Kausar, A. et al. Advent of alkali metal doping: a roadmap for the evolution of perovskite solar cells. *Chem. Soc. Rev.* **50**, 2696–2736 (2021).
- Li, Y. -h. et al. Review on the promising roles of alkali metals toward highly efficient perovskite light-emitting diodes. *J. Mater. Chem. C* **11**, 2011–2025 (2023).
- Wang, Z. et al. Suppressed phase segregation for triple-junction perovskite solar cells. *Nature* **618**, 74–79 (2023).
- Zhou, Y. et al. An ultrawide field-of-view pinhole compound eye using hemispherical nanowire array for robot vision. *Sci. Robot.* **9**, eadi8666 (2024).
- Qiu, X. et al. A tetrachromatic sensor for imaging beyond the visible spectrum in harsh conditions. *Device* **2**, 100357 (2024).
- Yi, C. et al. Entropic stabilization of mixed A-cation ABX<sub>3</sub> metal halide perovskites for high performance perovskite solar cells. *Energy Environ. Sci.* **9**, 656–662 (2016).
- Qiao, L., Fang, W.-H., Long, R. & Prezhdov, O. V. Extending carrier lifetimes in lead halide perovskites with alkali metals by passivating and eliminating halide interstitial defects. *Angew. Chem. Int. Ed.* **59**, 4684–4690 (2020).
- Li, Y. et al. Lattice modulation of alkali metal cations doped Cs<sub>1-x</sub>Rb<sub>x</sub>PbBr<sub>3</sub> halides for inorganic perovskite solar cells. *Sol. RRL* **2**, 1800164 (2018).
- Wang, Y.-K. et al. All-inorganic quantum-dot LEDs based on a phase-stabilized α-CsPbI<sub>3</sub> perovskite. *Angew. Chem. Int. Ed.* **60**, 16164–16170 (2021).
- Guo, Z. et al. Promoting energy transfer via manipulation of crystallization kinetics of quasi-2D perovskites for efficient green light-emitting diodes. *Adv. Mater.* **33**, 2102246 (2021).
- Cai, L. et al. Efficient and bright pure-blue all-inorganic perovskite light-emitting diodes from an ecofriendly alloy. *J. Phys. Chem. Lett.* **12**, 1747–1753 (2021).
- Nam, J. K. et al. Potassium Incorporation for enhanced performance and stability of fully inorganic cesium lead halide perovskite solar cells. *Nano Lett.* **17**, 2028–2033 (2017).
- Zhang, C. et al. Dual metal-assisted defect engineering towards high-performance perovskite solar cells. *Adv. Funct. Mater.* **32**, 2208077 (2022).
- Yang, J.-N. et al. Potassium bromide surface passivation on CsPbI<sub>3</sub>-xBr<sub>x</sub> nanocrystals for efficient and stable pure red perovskite light-emitting diodes. *J. Am. Chem. Soc.* **142**, 2956–2967 (2020).
- Hoang, M. T. et al. Potassium doping to enhance green photo-emission of light-emitting diodes based on CsPbBr<sub>3</sub> perovskite nanocrystals. *Adv. Optical Mater.* **8**, 2000742 (2020).
- Abdi-Jalebi, M. et al. Potassium- and rubidium-passivated alloyed perovskite films: optoelectronic properties and moisture stability. *ACS Energy Lett.* **3**, 2671–2678 (2018).
- Kuai, L. et al. Passivating crystal boundaries with potassium-rich phase in organic halide perovskite. *Sol. RRL* **3**, 1900053 (2019).
- Wang, L. et al. Potassium-induced phase stability enables stable and efficient wide-bandgap perovskite solar cells. *Sol. RRL* **4**, 2000098 (2020).
- Cao, J., Tao, S. X., Bobbert, P. A., Wong, C.-P. & Zhao, N. Interstitial occupancy by extrinsic alkali cations in perovskites and its impact on ion migration. *Adv. Mater.* **30**, 1707350 (2018).
- Kim, D. et al. Investigation of potassium doping and defect healing mechanism in core-shell CsPbBr<sub>3</sub>/SiO<sub>2</sub> quantum dots. *J. Mater. Chem. C* **12**, 6395–6405 (2024).



23. Liu, Y. et al. Considerably enhanced exciton emission of CsPbCl<sub>3</sub> perovskite quantum dots by the introduction of potassium and lanthanide ions. *Nanoscale* **10**, 14067–14072 (2018).
24. El Ajjouri, Y., Chirvony, V. S., Sessolo, M., Palazon, F. & Bolink, H. J. Incorporation of potassium halides in the mechanosynthesis of inorganic perovskites: feasibility and limitations of ion-replacement and trap passivation. *RSC Adv.* **8**, 41548–41551 (2018).
25. Shao, G. et al. KxCs<sub>1-x</sub>PbBr<sub>3</sub> NCs glasses possessing super optical properties and stability for white light emitting diodes. *Chem. Eng. J.* **375**, 122031 (2019).
26. Chu, Y. et al. Unveiling the photoluminescence regulation of colloidal perovskite quantum dots via defect passivation and lattice distortion by potassium cations doping: not the more the better. *J. Colloid Interface Sci.* **596**, 199–205 (2021).
27. Cao, Y. B. et al. High-efficiency, flexible and large-area red/green/blue all-inorganic metal halide perovskite quantum wires-based light-emitting diodes. *Nat. Commun.* **14**, 4611 (2023).
28. Hu, Y., Aygüler, M. F., Petrus, M. L., Bein, T. & Docampo, P. Impact of rubidium and cesium cations on the moisture stability of multiple-cation mixed-halide perovskites. *ACS Energy Lett.* **2**, 2212–2218 (2017).
29. Fu, Y. et al. Strongly quantum-confined perovskite nanowire arrays for color-tunable blue-light-emitting diodes. *ACS Nano* **16**, 8388–8398 (2022).
30. Waleed, A. et al. All inorganic cesium lead iodide perovskite nanowires with stabilized cubic phase at room temperature and nanowire array-based photodetectors. *Nano Lett.* **17**, 4951–4957 (2017).
31. Gu, L. et al. Significantly improved black phase stability of FAPbI<sub>3</sub> nanowires via spatially confined vapor phase growth in nanoporous templates. *Nanoscale* **10**, 15164–15172 (2018).
32. Schwartz, T., Bartal, G., Fishman, S. & Segev, M. Transport and Anderson localization in disordered two-dimensional photonic lattices. *Nature* **446**, 52–55 (2007).
33. Han, D. et al. Tautomeric mixture coordination enables efficient lead-free perovskite LEDs. *Nature* **622**, 493–498 (2023).
34. Subedi, B. et al. Urbach energy and open-circuit voltage deficit for mixed anion–cation perovskite solar cells. *ACS Appl. Mater. Interfaces* **14**, 7796–7804 (2022).
35. Fu, Y. et al. Scalable all-evaporation fabrication of efficient light-emitting diodes with hybrid 2D–3D perovskite nanostructures. *Adv. Funct. Mater.* **30**, 2002913 (2020).
36. Kim, J. S. et al. Ultra-bright, efficient and stable perovskite light-emitting diodes. *Nature* **611**, 688–694 (2022).
37. Xing, G. et al. Transcending the slow bimolecular recombination in lead-halide perovskites for electroluminescence. *Nat. Commun.* **8**, 14558 (2017).
38. Kagan, C. R. & Murray, C. B. Charge transport in strongly coupled quantum dot solids. *Nat. Nanotechnol.* **10**, 1013–1026 (2015).
39. Chen, M.-Y. et al. Strongly coupled tin-halide perovskites to modulate light emission: tunable 550–640 nm light emission (FWHM 36–80 nm) with a quantum yield of up to 6.4%. *Adv. Mater.* **30**, 1706592 (2018).
40. Zhang, D. et al. Large-scale planar and spherical light-emitting diodes based on arrays of perovskite quantum wires. *Nat. Photonics* **16**, 284–290 (2022).
41. Luo, X. et al. Effects of local compositional heterogeneity in mixed halide perovskites on blue electroluminescence. *Matter* **7**, 1054–1070 (2024).
42. Zhang, Q. et al. Light out-coupling management in perovskite LEDs—what can we learn from the past?. *Adv. Funct. Mater.* **30**, 2002570 (2020).

## Acknowledgements

This work was financially supported by Hong Kong Research Grant Council (General Research Fund Project No. 16205321, 16309018, and 16214619), HKUST Fund of Nanhai (Grant No. FSNH-18FYTR101),

Guangdong-Hong Kong-Macau Intelligent Micro-Nano Optoelectronic Technology Joint Laboratory (Grant No. 2020B1212030010), Foshan Innovative and Entrepreneurial Research Team Program (2018IT100031), NSFC/RGC Joint Research Scheme Funding N\_HKUST657/22. National Natural Science Foundation of China (NSFC-RGC 62261160392 and 52131304), Zhongshan Municipal Science and Technology Bureau (ZSST21EG05). The authors also acknowledge the support from the Material Characterization and Preparation Facility (MCPF) and the Center for 1D/2D Quantum Materials and the State Key Laboratory on Advanced Displays and Optoelectronics Technologies at HKUST.

## Author contributions

Z.F. and Y.C. initiated the study and designed the experiments. Y.C. carried out PeQWs and LED device fabrication, optical characterization and measured device's performance. X.Q., W.T., Q.S. and H.Z. carried out SEM and TEM characterizations. J.L. and D.K. performed TA measurements. K.Z. and Y.L. conducted XRD measurements. Z.J. and J.W. conducted the temperature-dependent PL measurements. P.C. and X.L. carried out GIWAXS measurements. F.Y. and Y.X. did theoretical calculations. Y.C. and Q.Z. performed FDTD simulation. X.Q. and X.S. provided support for characterization of the materials. F.X. performed aluminum sputtering. B.R. and D.Z. assisted with the measurement of LED devices. Y.C. and Y.Z. analyzed data and organized the figure. Y.C. drafted the first version of the manuscript, with assistance from Y.Z., Y.F., D.Z., Y.D. and Z.F. All authors discussed the results and commented on the manuscript.

## Competing interests

The authors declare no competing interests.

## Additional information

**Supplementary information** The online version contains supplementary material available at <https://doi.org/10.1038/s41467-025-61085-6>.

**Correspondence** and requests for materials should be addressed to Haibo Zeng or Zhiyong Fan.

**Peer review information** *Nature Communications* thanks Jiajun Luo and the other anonymous reviewer(s) for their contribution to the peer review of this work. A peer review file is available.

**Reprints and permissions information** is available at <http://www.nature.com/reprints>

**Publisher's note** Springer Nature remains neutral with regard to jurisdictional claims in published maps and institutional affiliations.

**Open Access** This article is licensed under a Creative Commons Attribution-NonCommercial-NoDerivatives 4.0 International License, which permits any non-commercial use, sharing, distribution and reproduction in any medium or format, as long as you give appropriate credit to the original author(s) and the source, provide a link to the Creative Commons licence, and indicate if you modified the licensed material. You do not have permission under this licence to share adapted material derived from this article or parts of it. The images or other third party material in this article are included in the article's Creative Commons licence, unless indicated otherwise in a credit line to the material. If material is not included in the article's Creative Commons licence and your intended use is not permitted by statutory regulation or exceeds the permitted use, you will need to obtain permission directly from the copyright holder. To view a copy of this licence, visit <http://creativecommons.org/licenses/by-nc-nd/4.0/>.

© The Author(s) 2025